

# CP violating effects in coherent elastic neutrino-nucleus scattering processes

D. Aristizabal Sierra,<sup>1,2,\*</sup> V. De Romeri,<sup>3,†</sup> and N. Rojas<sup>1,‡</sup>

<sup>1</sup>*Universidad Técnica Federico Santa María - Departamento de Física  
Casilla 110-V, Avda. España 1680, Valparaíso, Chile*

<sup>2</sup>*IFPA, Dep. AGO, Université de Liège, Bat B5, Sart Tilman B-4000 Liège 1, Belgium*

<sup>3</sup>*AHEP Group, Instituto de Física Corpuscular, CSIC/Universitat de València,  
Calle Catedrático José Beltrán, 2 E-46980 Paterna, Spain*

The presence of new neutrino-quark interactions can enhance, deplete or distort the coherent elastic neutrino-nucleus scattering (CEvNS) event rate. The new interactions may involve CP violating phases that can potentially affect these features. Assuming light vector mediators, we study the effects of CP violation on the CEvNS process in the COHERENT sodium-iodine, liquid argon and germanium detectors. We identify a region in parameter space for which the event rate always involves a dip and another one for which this is never the case. We show that the presence of a dip in the event rate spectrum can be used to constraint CP violating effects, in such a way that the larger the detector volume the tighter the constraints. Furthermore, it allows the reconstruction of the effective coupling responsible for the signal with an uncertainty determined by recoil energy resolution. In the region where no dip is present, we find that CP violating parameters can mimic the Standard Model CEvNS prediction or spectra induced by real parameters. We point out that the interpretation of CEvNS data in terms of a light vector mediator should take into account possible CP violating effects. Finally, we stress that our results are qualitatively applicable for CEvNS induced by solar or reactor neutrinos. Thus, the CP violating effects discussed here and their consequences should be taken into account as well in the analysis of data from multi-ton dark matter detectors or experiments such as CONUS, v-cleus or CONNIE.

## I. INTRODUCTION

Coherent elastic neutrino-nucleus scattering (CEvNS) is a process that occurs when the de Broglie wavelength  $\lambda$  of the scattering process is larger than the nuclear radius. In terms of the exchanged momentum  $q$  this means that when  $q \lesssim h/r_N \simeq 100 \text{ MeV}$  the individual nucleonic amplitudes sum up coherently. As a consequence the total amplitude gets enhanced by the number of nucleons, resulting in a rather sizable cross section. Indeed, among all possible scattering processes at neutrino energies below 100 MeV, CEvNS has the largest cross section. Measuring CEvNS however is challenging due to the small nuclear recoil energies involved. The first measurement was done in 2017 by the COHERENT experiment, which observed the process at a  $6.7\sigma$  confidence level (CL), using neutrinos produced in the Oak Ridge National Laboratory Spallation Neutron Source [1].

Given the constraints on the neutrino energy probe, CEvNS can be induced by neutrinos produced in fixed target experiments such as in COHERENT, reactor neutrinos and solar and atmospheric neutrinos. Within the second category CONUS is an ongoing experiment [2] and there are as well other experimental proposals that aim at using reactor neutrinos to measure CEvNS using different technologies [3, 4]. Relevant for the third category are direct detection multi-ton dark matter (DM) experiments such as XENONnT, LZ and DARWIN [5–7]. There is clearly a great deal of experimental interest on CEvNS, in particular for the role it will play in near-future DM direct detection experiments [8, 9] and the different physics opportunities it offers in these facilities [10–16].

From the phenomenological point of view, it is therefore crucial to understand the different uncertainties the process involves and the impact that new physics effects might have on the predicted spectra.

The Standard Model (SM) CEvNS cross section proceeds through a neutral current process [17, 18]<sup>1</sup>. Depending on the target nucleus, in particular for heavy nuclei, it can involve sizable uncertainties arising mainly from the root-mean-square radius of the neutron density distribution [20]. However, apart from this nuclear physics effect the SM provides rather definitive predictions for CEvNS on different nuclear targets. Precise measurements of the process offer a tool that can be used to explore the presence of new physics effects. In fact, since the COHERENT data release [1, 21], various analyses involving new physics have been carried out. The scenarios considered include effective neutrino non-standard interactions [22–24], light vector and scalar mediators [23, 25], neutrino electromagnetic properties [26, 27], sterile neutrinos [26] and neutrino generalized interactions [28].

Analyses of new physics so far have considered CP conserving physics. This is mainly motivated by simplicity and—arguably—because at first sight one might think that getting information on CP violating interactions in CEvNS experiments is hard, if possible at all. CP violating effects are typically studied through observables that depend on asymmetries that involve states and anti-states or polarized beams, which in a CEvNS experiment are challenging to construct. In this paper we show that information on CP violating interactions can be obtained in a different way through the features they induce on the event rate spectrum, and for that aim we consider light vector mediator scenarios (with masses  $m_V \lesssim 100 \text{ MeV}$ ).

\* daristizabal@ulg.ac.be

† deromeri@ific.uv.es

‡ nicolas.rojasro@usm.cl

<sup>1</sup> Recently this cross section has been revisited and the incoherent neutrino-nucleus elastic cross section has been recalculated in [19].

Phenomenologically, among the possible new degrees of freedom that can affect CEvNS, light vectors are probably the most suitable. In contrast to heavy vectors, they are readily reconcilable with constraints from the charged lepton sector, while at the same time leading to rather sizable effects [29]. In contrast to light scalar mediators, they interfere with the SM contribution and can eventually lead to a full cancellation of the event rate at a specific nuclear recoil energy. This is a feature of particular relevance in the identification of CP violating effects, as we will show.

In our analysis we use the COHERENT germanium (Ge), sodium (Na) and liquid argon (LAR) detectors to show the dependence of CP violating effects on target materials and detector volumes. We fix the detector parameters according to future prospects [30] and in each case we extract information of CP violation by comparing CP conserving and CP violating event rate spectra (induced by real or complex parameters). We then establish the reach of each detector to constrain CP violating effects by performing a  $\chi^2$  analysis.

The rest of the paper is organized as follows. In sec. II we fix the interactions, the notation and we introduce the parametrization that will be used throughout our analysis. In sec. III we present the parameter space analysis, we discuss constraints on light vector mediators and identify CP violating effects. In sec. IV we discuss the possible limits that the sodium, germanium and argon detectors could eventually establish on CP violating effects. Finally, in sec. V we summarize our results.

## II. CP VIOLATING INTERACTIONS

Our analysis is done assuming that the new physics corresponds to the introduction of light vector mediators. This choice has to do with phenomenological constraints. Although subject to quite a few number of limits, models for such scenarios already exist [31]. They are not only phenomenologically consistent, but they also allow for large effects in a vast array of experiments [32, 33]. In contrast, in heavy mediator models the constraints from the charged lepton sector lead—in general—to effective couplings whose effects barely exceed few percent [34].

We allow for neutrino vector and axial currents, while for quarks we only consider vector interactions (axial quark currents are spin suppressed), and we assume that all couplings are complex at the renormalizable level. The Lagrangian of the new physics can then be written according to

$$\mathcal{L} = f_V \bar{\nu} \gamma_\mu \nu V^\mu + i f_A \bar{\nu} \gamma_\mu \gamma_5 \nu V^\mu + \sum_{q=u,d} h_V^q \bar{q} \gamma_\mu q V^\mu, \quad (1)$$

where  $f_V = |f_V| e^{i\phi_V}$ ,  $f_A = |f_A| e^{i\phi_A}$ ,  $h_V^q = |h_V^q| e^{i\phi_{Vq}}$ , we have dropped lepton flavor indices and we restrict the sum to first generation quarks. In terms of the “fundamental” parameters the nuclear vector current coupling reads (with explicit dependence on the transferred momentum  $q$ )

$$h_V(q^2) = N \left( 2h_V^d + h_V^u \right) F_n(q^2) + Z \left( h_V^d + 2h_V^u \right) F_p(q^2), \quad (2)$$

where  $N = A - Z$ , with  $A$  and  $Z$  the mass and atomic number of the corresponding nuclide.  $F_{n,p}(q^2)$  are the neutron and proton nuclear form factors obtained from the Fourier transform of the nucleonic density distributions (in the first Born approximation). Note that this differentiation is particularly relevant for nuclides with  $N > Z$ , such as sodium, argon or germanium [20].

The interactions in (1) affect CEvNS processes, as they introduce a  $q$  dependence, absent in the SM, that changes the recoil energy spectrum and can either enhance or deplete the expected number of events. Here we will consider both mono- and multi-target detectors, and so we write the CEvNS cross section for the  $i^{\text{th}}$  isotope:

$$\frac{d\sigma}{dE_r} = \frac{G_F^2 m_i}{2\pi} |\xi_V(q_i^2)|^2 \left( 2 - \frac{E_r m_i}{E_\nu^2} - \frac{2E_r}{E_\nu} + \frac{E_r^2}{E_\nu^2} \right). \quad (3)$$

Here  $m_i$  refers to the isotope’s atomic mass and  $q_i^2 = 2m_i E_r$ , where  $E_r^{\text{max}} \simeq 2E_\nu^2/m_i$ ,  $E_\nu$  being the energy of the incoming neutrino. The overall energy-dependent factor  $\xi_V(q_i^2)$  encodes the CP violating physics and reads

$$\xi_V(q_i^2) = g_V(q_i^2) - \frac{h_V(q_i^2)(f_V - i f_A)}{\sqrt{2} G_F (q_i^2 - m_V^2)}, \quad (4)$$

with  $g_V(q^2)$  the SM contribution weighted properly by the nuclear form factors, namely

$$g_V(q_i^2) = N \left( 2g_V^d + g_V^u \right) F_n(q^2) + Z \left( g_V^d + 2g_V^u \right) F_p(q^2), \quad (5)$$

with  $g_V^u = 1/2 - 4/3 \sin^2 \theta_W$  and  $g_V^d = -1/2 + 2/3 \sin^2 \theta_W$ . For the weak mixing angle we use the central value obtained using the  $\overline{\text{MS}}$  renormalization scheme and evaluated at the  $Z$  boson mass,  $\sin^2 \theta_W = 0.23122$  [35].

Typical nuclear form factors parametrizations depend on two parameters which are constrained via the corresponding nucleonic density distribution root-mean-square (rms) radii. For a large range of nuclides, proton rms radii have been precisely extracted from a variety of experiments [36]. Consequently, uncertainties on  $F_p(q^2)$  are to a large degree negligible. In contrast, neutron rms radii are poorly known and so uncertainties on  $F_n(q^2)$  can be large. These uncertainties have been recently studied in [20] by assuming that  $r_{\text{rms}}^n \subset [r_{\text{rms}}^p, r_{\text{rms}}^p + 0.3 \text{ fm}]$  (for heavy nuclei). The lower bound is well justified in nuclides with  $N > Z$ , while the upper one is limited by constraints from neutron skin thickness [37]. In our analysis we choose to fix  $r_{\text{rms}}^n = r_{\text{rms}}^p$  and use the same form factor parametrization (Helm form factor [38]) for both, neutrons and protons [20]. Doing so, the  $q^2$  dependence of the parameter in (4) comes entirely from the denominator in the second term and that enables a simplification of the multi-parameter problem. Note that we do not consider form factor uncertainties in order to avoid mixing their effects with the CP violating effects we want to highlight.

In general the analysis of CP violating effects is a nine parameter problem: the vector boson mass, four moduli and four CP phases. However, the problem can be reduced to three parameters by rewriting the product of the nuclear and neutrino complex couplings in the second term in (4) in terms of

real and complex components. A moduli  $|H_V|^2 = \Re(H_V)^2 + i\Im(H_V)^2$  a phase  $\tan\phi = \Im(H_V)/\Re(H_V)$  and the vector boson mass. In terms of the fundamental couplings and CP phases, they are given by

$$\begin{aligned}\Re(H_V) &= 2(f_V + f_A) \sum_{q=u,d} \mathcal{A}_q h_V^q \sin(\alpha/4) \sin(\beta_+^q/4), \\ \Im(H_V) &= 2(f_A - f_V) \sum_{q=u,d} \mathcal{A}_q h_V^q \sin(\alpha/4) \sin(\beta_-^q/4),\end{aligned}\quad (6)$$

with  $\mathcal{A}_d = 2A - Z$ ,  $\mathcal{A}_u = Z + A$ ,  $\alpha = \pi + 2(\phi_A - \phi_V)$  and  $\beta_{\pm}^q = \pi \pm 2(\phi_A + \phi_V + 2\phi_{Vq})$ . Proceeding in this way the cross section then depends on  $m_V$ ,  $|H_V|$  and  $\phi$  through the parameter  $\xi_V$  in (4), that is now simplified to

$$\xi_V = g_V + \frac{|H_V|e^{i\phi}}{\sqrt{2}G_F(2m_i E_r + m_V^2)}. \quad (7)$$

One can see that the cross section is invariant under  $\phi \rightarrow -\phi$ , so the analysis can be done by considering  $\phi \in [0, \pi]$ . The phase reflection invariance of the cross section assures that the results obtained for such interval hold as well for  $\phi \in [-\pi, 0]$ . The boundaries of this interval define the two CP conserving cases of our analysis. Since  $g_V$  is always negative,  $\phi = 0$  always produces destructive interference between the SM and the light vector contribution. At the recoil spectrum level this translates into a depletion of the SM prediction in a certain recoil energy interval. In contrast,  $\phi = \pi$  implies always constructive interference, and so an enhancement of the recoil spectrum above the SM expectation.

It becomes clear as well that the conclusions derived in terms of  $|H_V|$  and  $\phi$  can then be mapped into the eight-dimensional parameter space spanned by the set  $\{|f_{V,A}|, |h_V^q|, \phi_{V,A}, \phi_{Vq}\}$ .

### III. EVENT RATES, CONSTRAINTS AND PARAMETER SPACE ANALYSIS

To characterize CP violating effects we consider CEVNS produced by fixed target experiments, in particular at COHERENT. Qualitatively, the results derived here apply as well in the case of CEVNS induced by reactor and solar ( $^8\text{B}$ ) neutrinos. We start the analysis by studying the effects in mono-target sodium ( $^{23}\text{Na}$ )<sup>2</sup> and argon ( $^{40}\text{Ar}$ ) detectors and then consider the case of a multi-target germanium detector. For the latter case one has to bear in mind that germanium has five stable isotopes  $^{70}\text{Ge}$ ,  $^{72}\text{Ge}$ ,  $^{73}\text{Ge}$ ,  $^{74}\text{Ge}$  and  $^{76}\text{Ge}$  with relative abundances 20.4%, 27.3%, 7.76%, 36.7% and 7.83%, respectively.

In the multi-target case the contribution of the  $i^{\text{th}}$  isotope to the energy recoil spectrum can be written according to [20]

$$\frac{dR_i}{dE_r} = \frac{m_{\text{det}} N_A}{\langle m \rangle} \int_{E_r^{\text{min}}}^{E_r^{\text{max}}} \Phi(E_\nu) X_i \frac{d\sigma_i}{dE_r} F_H^2(q_i^2) dE_\nu, \quad (8)$$

where  $m_{\text{det}}$  is the detector mass in kg,  $\langle m \rangle = \sum_k X_k m_k$  with  $m_k$  the  $k^{\text{th}}$  isotope molar mass measured in kg/mol,  $X_i$  is the isotope relative natural abundance,  $N_A = 6.022 \times 10^{23} \text{ mol}^{-1}$ ,  $\Phi(E_\nu)$  the neutrino flux and  $F_H^2(q_i^2)$  stands for the Helm form factor. The integration limits are  $E_r^{\text{max}} = m_\mu/2$  (for a fixed-target experiment like COHERENT) and  $E_r^{\text{min}} = \sqrt{m_i E_r}/2$ . The full recoil spectrum then results from  $dR/dE_r = \sum_i dR_i/dE_r$ . Note that (8) reduces to the single target case when  $X_i = 1$  and  $m = m_k = 0.932A_k \text{ GeV}/c^2$ . The number of events in a particular detector is then calculated as

$$N_{\text{events}} = \int_{E_r - \Delta E_r}^{E_r + \Delta E_r} \frac{dR}{dE_r} \mathcal{A}(E_r) dE_r, \quad (9)$$

with  $\mathcal{A}(E_r)$  the acceptance function of the experiment. In our analyses we take  $\Delta E_r = 1.5 \text{ keV}$ .

#### A. Constraints on light vector mediators

Before proceeding with our analysis it is worth reviewing the constraints to which the light vector mediators we consider are subject to. These constraints arise from beam dump and fixed target experiments,  $e^+e^-$  colliders and LHC, lepton precision experiments, neutrino data as well as astrophysical observations [39]. From the collision of an electron or proton beam on a fixed target,  $V$  can be produced either through Bremsstrahlung or meson production and subsequent decay,  $\pi^0 \rightarrow \gamma + V$ . The interactions in (1) do not involve charged leptons, hence in the light mediator scenario here considered the coupling of  $V$  to electrons is loop suppressed. Limits from electron beam dump and fixed target experiments can be therefore safely ignored. Limits from proton beams are seemingly more relevant since the production of  $V$  is possible by Bremsstrahlung—through the vertex  $\bar{p}\gamma_\mu p V^\mu$ —or by meson decay. However, since these searches are based on  $V$  decay modes involving charged leptons, again the constraints are weakened by loop suppression factors.

The potential limits from  $e^+e^-$  collider searches (e.g. KLOE, BaBar or Belle-II [40–42]), from muon and tau rare decays (SINDRUM and CLEO [43, 44]) and from LHC searches (LHCb, ATLAS and CMS [45, 46]) are feeble due to the same argument, couplings of  $V$  to charged leptons are loop suppressed. As to the limits from neutrino scattering experiments, Borexino, neutrino trident production and TEXONO [10, 47, 48] involve couplings to charged leptons and so are weak too. Thus, from laboratory experiments the only relevant limit arises from COHERENT CsI phase [1], which have been studied in detail in ref. [23] under the assumption of real parameters. We thus update those limits by considering  $\phi \neq 0$ . To do so we follow the same strategy adopted in ref.

<sup>2</sup> Throughout the paper we refer to this case as NaI detector. The high-energy  $^{23}\text{Na}$  recoils have a better signal-to-background ratio than  $^{127}\text{I}$ , and so CEVNS is measured in  $^{23}\text{Na}$ . Iodide is instead employed to measure  $\nu_e$ -induced charged current processes [21]. Thus, from the CEVNS point of view NaI is a mono-target experiment.

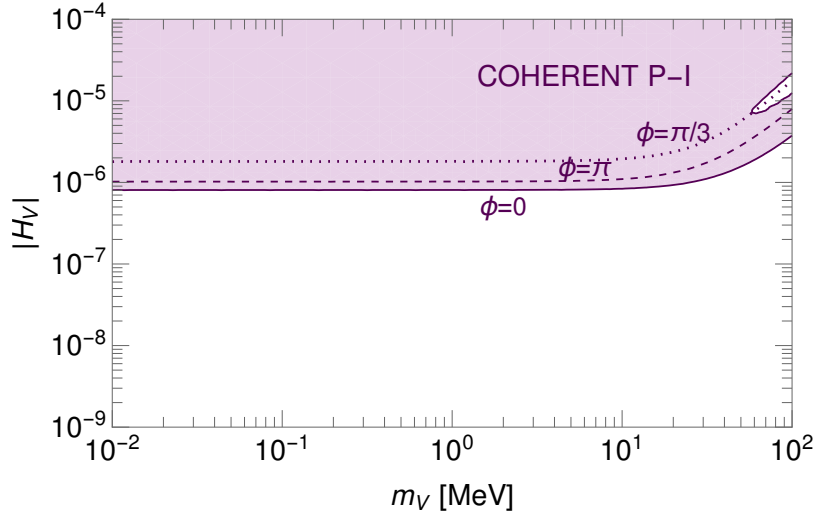


FIG. 1. Bounds on vector light mediators derived from COHERENT P-I data. The bounds include the real cases  $\phi = 0$  and  $\phi = \pi$  as well as  $\phi = \pi/3$ , value for which the limit is found to be the less stringent.

[28]. First of all, we define the following spectral  $\chi^2$  function

$$\chi^2 = \sum_{i=1}^{16} \left( \frac{N_i^{\text{exp}} - (1 + \alpha)N_i^{\text{BSM}} - (1 + \beta)B_i^{\text{on}}}{\sigma_i} \right)^2 + \left( \frac{\alpha}{\sigma_\alpha} \right)^2 + \left( \frac{\beta}{\sigma_\beta} \right)^2, \quad (10)$$

where the binning runs over number of photoelectrons  $n_{\text{PE}}$  ( $\Delta n_{\text{PE}} = 2$  and  $n_{\text{PE}} = 1.17(E_r/\text{keV})$ ),  $\alpha$  and  $\beta$  are nuisance parameters,  $\sigma_i$  are experimental statistical uncertainties and  $\sigma_\alpha = 0.28$  and  $\sigma_\beta = 0.25$  quantify standard deviations in signal and background respectively. For the calculation of  $N_i^{\text{BSM}}$  we employ eqs. (8) and (9) adapted to include the Cs and I contributions, i.e.  $m_{\text{det}} = 14.6 \text{ kg}$ ,  $\langle m \rangle \rightarrow m_{\text{CsI}}$  ( $m_{\text{CsI}}$  the CsI molar mass) and  $X_i \rightarrow A_i/(A_{\text{Cs}} + A_{\text{I}})$ . For neutrino fluxes we use the following spectral functions

$$\begin{aligned} \mathcal{F}_{\nu_\mu}(E_\nu) &= \frac{2m_\pi}{m_\pi^2 - m_\mu^2} \delta \left( 1 - \frac{2E_\nu m_\pi}{m_\pi^2 - m_\mu^2} \right), \\ \mathcal{F}_{\nu_e}(E_\nu) &= \frac{192}{m_\mu} \left( \frac{E_\nu}{m_\mu} \right)^2 \left( \frac{1}{2} - \frac{E_\nu}{m_\mu} \right), \\ \mathcal{F}_{\bar{\nu}_\mu}(E_\nu) &= \frac{64}{m_\mu} \left( \frac{E_\nu}{m_\mu} \right)^2 \left( \frac{3}{4} - \frac{E_\nu}{m_\mu} \right), \end{aligned} \quad (11)$$

normalized according to  $\mathcal{N} = r \times n_{\text{POT}}/4/\pi/L^2$ , with  $r = 0.08$ ,  $n_{\text{POT}} = 1.76 \times 10^{23}$  and  $L = 19.3 \text{ m}$ . The result is displayed in fig. 1 where it can be seen that the inclusion of CP phases relaxes the bound. We found that the less stringent limit is obtained for  $\phi = \pi/3$ , which is about a factor 2.5 larger than the bound obtained at  $\phi = 0$ .

The last limits which apply in our case are of astrophysical origin. Particularly important are horizontal branch stars which have a burning helium core with  $T \simeq 10^8 \text{ K} \simeq 10^{-2} \text{ MeV}$ . In such an environment vector bosons with masses

of up to  $10^{-1} \text{ MeV}$  (from the tail of the thermal distribution) can be produced through Compton scattering processes  $\gamma + {}^4\text{He} \rightarrow V + {}^4\text{He}$  which lead to energy loss. Consistency with the observed number ratio of horizontal branch stars in globular clusters leads to a constraint on the vector-nucleon couplings  $h_V^{p,n} \lesssim 4 \times 10^{-11}$  [49, 50]. Assuming  $h_V^p = h_V^n$  this bound can be translated into  $|H_V| = \sqrt{2} A h_V^n \lesssim 6 \times 10^{-11} A$ . Relevant as well are the bounds derived from supernova, which exclude regions in parameter space for light vector boson masses up to  $\sim 100 \text{ MeV}$ <sup>3</sup>. Neutrinos are trapped in the supernova core, so they can only escape by diffusion. Consistency with observations implies  $t_{\text{diff}} \sim 10 \text{ s}$ , therefore limits can be derived by requiring that the new interaction does not sizably disrupt  $t_{\text{diff}}$ . Further limits can be derived from energy-loss arguments if the new interactions open new channels for neutrino emission, which is the case in the scenario we are considering through  $V \rightarrow \bar{\nu} \nu$  (a process that resemble the plasma process  $\gamma \rightarrow \bar{\nu} \nu$ ). All these limits have been recently reviewed for dark photons in [52] and span a region of parameter space that covers several orders of magnitude in both  $|H_V|$  and  $m_V$ .

There are various considerations that have to be taken into account regarding these bounds. First of all, uncertainties on the behavior of core-collapse supernovae are still substantial [53]. As a result, limits from supernovae should be understood as order-of-magnitude estimations. The bounds from stellar cooling arguments discussed above neglect plasma mixing effects, which are relevant whenever the vector has an effective in-medium mixing with the photon. Taking into account these effects, the production rate of the new vectors in the stellar environment is affected, resulting in rather different bounds [54].

<sup>3</sup> Supernova temperatures are order  $T \simeq 30 \text{ MeV}$ , and so in that environment states with masses of up to  $\sim 100 \text{ MeV}$  can be produced if one consider the tail of the thermal distribution [51].

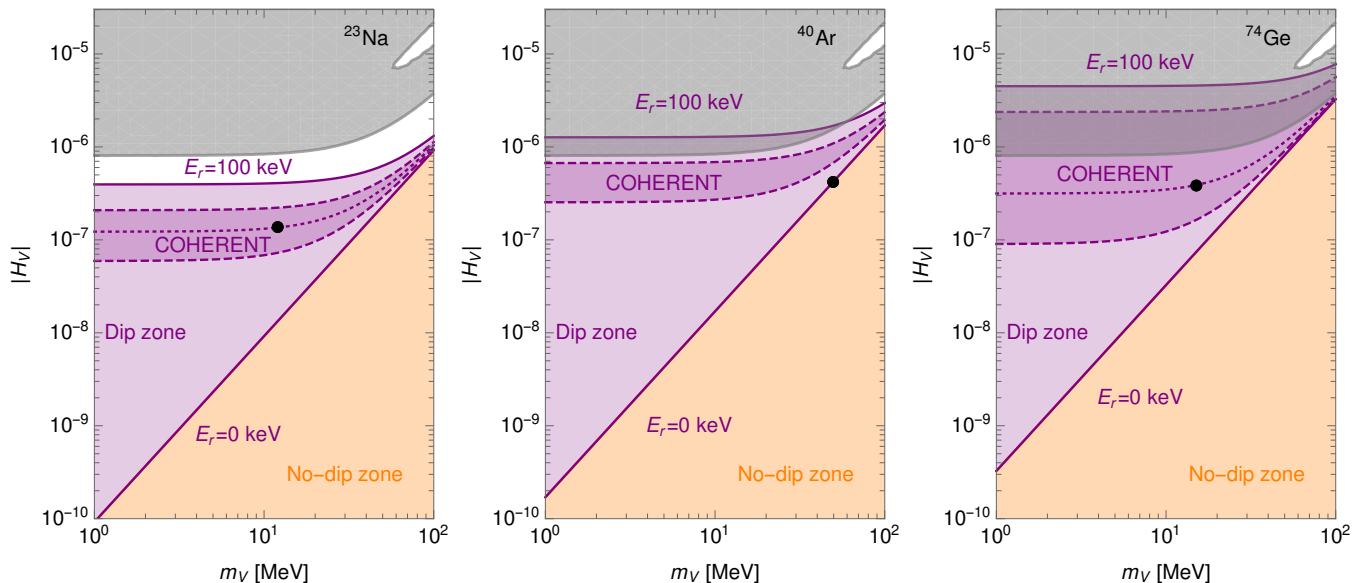


FIG. 2. Parameter space regions determined by the condition that the spectrum exhibits or not a dip at a given recoil energy, in  $^{23}\text{Na}$  (**left graph**),  $^{40}\text{Ar}$  (**middle graph**) and  $^{74}\text{Ge}$  (**right graph**). For parameters in the upper triangle (purple region) a dip in the event rate spectrum is always found, while this is not the case for parameters in the lower triangle (orange region). The plain and dashed/dotted curves are isocontours referring to increasing values of recoil energy, from  $E_r = 0$  (plain diagonal purple line) to  $E_r = 100$  keV (top plain purple line). The shaded regions labeled with COHERENT indicate the recoil energy regions of interest for the sodium, argon and germanium COHERENT detectors (see sec. III B for further details). The grey shaded area indicates the region already excluded by COHERENT P-I, assuming the real case  $\phi = 0$  (see Fig. 1).

Additional environmental effects can alter the bounds from stellar cooling as well as from supernova. This is the case when the vector couples to a scalar which condensates inside macroscopic objects, and screens the charge which  $V$  couples to [55, 56]. The vector mass in this scenario is proportional to the medium mass density  $\rho$ , and so in stellar and supernova environments (high-density environments) its production is no longer possible. In summary, astrophysical constraints should be considered with care as they largely depend on the assumptions used. Thus, for concreteness and because this is the window where new CP violating effects are more pronounced, we focus our analysis in the region  $m_V \subset [1, 100]$  MeV.

## B. Parameter space slicing

For CP conserving parameters a full cancellation of the SM contribution, at a given recoil energy, becomes possible in the case  $\phi = 0$ . In contrast, CP violating parameters do not allow such a possibility. For  $N_{\text{events}}$  such a cancellation leads to a dip at the recoil energy at which the cancellation takes place. Thus, such a feature in the spectrum will favor CP conserving new physics. Taking this into account, we then split the  $m_V - |H_V|$  plane in two “slices”: One for which the recoil spectrum will always exhibit a dip, and a second one for which this is never the case, regardless of  $\phi$ . The boundary of such regions is clearly determined by the condition that the parameter in eq. (7) vanishes, which translates into a relation between  $|H_V|$

and  $m_V$  for a fixed recoil energy, namely

$$|H_V| = -\sqrt{2}g_V G_F (2m_i E_r + m_V^2). \quad (12)$$

In a mono-target experiment the cancellation is exact at a given energy, but in a multi-target detector this is clearly not the case. However, as we will later show in sec. IV A the cancellation is still good enough so to be used to distinguish the CP conserving case from the CP violating one. One can see as well that the position of the dips implied by eq. (12) depends on the type of isotope considered, so different nuclides span different portions of parameter space. This can be seen in fig. 2 in which the parameter space regions  $m_V - |H_V|$  are displayed for  $^{23}\text{Na}$ ,  $^{40}\text{Ar}$  and  $^{74}\text{Ge}$ .

The regions labeled with COHERENT refer to the energy regions of interest in each case. In all three cases the upper energy isocontour is fixed as  $E_r = 50$  keV (determined by the  $\nu_e$  flux kinematic endpoint), and the lower isocontour according to the projected detector recoil energy thresholds. For the NaI detector we assume  $E_r^{\text{th}} = 15$  keV, for the LAr  $E_r^{\text{th}} = 20$  keV and for germanium  $E_r^{\text{th}} = 2$  keV. The lower isocontour at  $E_r = 0$  keV defines the boundary of the regions with distinctive and not overlapping CP violating features: dips and degeneracies. The upper isocontour at  $E_r = 100$  keV is fixed by the condition of keeping the elastic neutrino-nucleus scattering coherent. Apart from these particular energy isocontours, any other one within the dip zone determines the position of the dip. This means that if future data will show a dip in the event spectrum, and one interprets such a dip in terms of a

Detector	Detector mass [kg]	Distance from source [m]	Threshold [keV]
Sodium	2000	28	15
Liquid Argon	1000	29	20
Germanium	15	22	2

TABLE I. Main detector parameters employed in our analysis, taken from [30]. For the number of protons on target  $n_{\text{POT}}$  we have extrapolated the value of the CsI phase to one year in all cases,  $n_{\text{POT}} = (365/308.1)1.76 \times 10^{23} = 2.1 \times 10^{23}$ . Acceptances  $\mathcal{A}(E_r)$  are taken as Heaviside functions at the energy thresholds specified in the fourth column.

light vector mediator scenario, its energy location will provide valuable information about the new physics parameters.

To emphasize this observation we consider the  $^{23}\text{Na}$  mono-target detector as well as the germanium multi-target detector. In the first case, we consider the parameter space point  $\{m_V, |H_V|\} = \{12\text{MeV}, 1.32 \times 10^{-7}\}$  as indicated in the left panel of fig. 2 with a black point. That point is located along the  $E_r = 31\text{keV}$  dotted isocontour, so with  $\phi = 0$  a dip in that position is found as shown in the upper left graph in fig. 3 (detector parameters used for this calculation can be seen in tab. I). Data from that detector will identify its exact location up to bin size (energy resolution). Assuming  $\Delta E_r = 1.5\text{keV}$ , such a spectrum will allow to determine  $|H_V|$  with a 4% accuracy within the range  $[1.22 \times 10^{-7}, 1.04 \times 10^{-6}]$  obtained at  $m_V = 1\text{MeV}$  and  $m_V = 100\text{MeV}$ , respectively.

As the upper left panel in fig. 3 shows, the presence of CP violating phases produces departures from the dip and so—in principle—one can relate the amount of CP violation to the dip depth. In a mono-target detector this behavior is rather clear given that the dip is related with a cancellation in a single isotope. In a multi-target detector such as for germanium this is not entirely clear. So let us discuss this in more detail. The event rate spectrum is obtained from five different contributions, according to eq. (8). Cancellation at a certain recoil energy for a specific isotope requires a precise value of  $H_V$  determined by the isotope mass and mass number, and so one expects the remaining contributions not to cancel at that energy.

To investigate what happens in this case, we take the parameter space point  $\{m_V, |H_V|\} = \{15\text{MeV}, 4.17 \times 10^{-7}\}$ , located along the  $E_r = 7\text{keV}$  isocontour for  $^{74}\text{Ge}$ , as indicated in the right graph in fig. 2 with the black point. For that point, the quantity  $\widehat{\sigma}_i = X_i (d\sigma_i/dE_r) F_H^2(q_i)$  exactly cancels for  $^{74}\text{Ge}$  and  $E_V = 50\text{MeV}$  (any other value allowed by the kinematic criterion  $E_V > \sqrt{m_i E_r/2}$  will lead to the same conclusion). For the remaining isotopes, instead, the following values are found

$$\begin{aligned} \widehat{\sigma}_{70} &= 1.5 \times 10^{-39} \frac{\text{cm}^2}{\text{MeV}}, & \widehat{\sigma}_{72} &= 5.1 \times 10^{-40} \frac{\text{cm}^2}{\text{MeV}}, \\ \widehat{\sigma}_{73} &= 3.6 \times 10^{-41} \frac{\text{cm}^2}{\text{MeV}}, & \widehat{\sigma}_{76} &= 1.4 \times 10^{-40} \frac{\text{cm}^2}{\text{MeV}}, \end{aligned} \quad (13)$$

which certainly are rather sizable. The key observation here is that for the same parameter space point all five isotopes generate a dip within a recoil energy interval of 2keV. More precisely, at  $E_r = 8.4\text{keV}$ ,  $E_r = 7.6\text{keV}$ ,  $E_r = 7.3\text{keV}$ ,  $E_r = 6.4\text{keV}$  for  $^{70}\text{Ge}$ ,  $^{72}\text{Ge}$ ,  $^{73}\text{Ge}$ ,  $^{76}\text{Ge}$  respectively. Thus, given

the spread of those dipoles, the event rate spectrum does involve a rather pronounced depletion that looks like the dip found in a mono-target detector.

Note that the reason behind the appearance of multiple dipoles from different germanium isotopes has to do with their similarity. The value of  $|H_V|$  for a fixed vector boson mass is entirely determined by  $m_i$  and  $A_i$  through eq. (12). Once the value of  $|H_V|$  is fixed using the mass and mass number of a particular isotope (in this particular case  $^{74}\text{Ge}$ ), eq. (12) fixes as well the points at which the remaining dipoles will appear. The different recoil energy positions differ only by the relative values of  $g_V^i$  and  $m_i$  compared to those of the isotope that has been used to fix  $|H_V|$ . For  $^{70}\text{Ge}$  these differences are order 10% and 5%, while for  $^{76}\text{Ge}$  they are 5% and 2%. Since the differences for  $^{70}\text{Ge}$  are the largest, for this isotope one finds the largest shift from  $E_r = 7\text{keV}$ . Moreover, since the differences in all cases are small, the spread of the dipoles is small as well. This conclusion is therefore independent of the parameter space point chosen: *There exists as well a dip zone in a multi-target detector (in this case, Germanium based), for which given a point in it the event rate spectrum will always exhibit a dip.*

This behavior can be seen in the upper right graph in fig. 3. The overall dip is a result of the five contributions and of their dipoles spreading over a small recoil energy window around  $\sim 7\text{keV}$ . One can see as well that the presence of CP violating phases has the same effect that in a mono-target detector. As soon as they are switched on, departures from the dip are seen, and the behavior is such that large  $\phi$  tends to soften the dip. At this point it is therefore clear that in both, mono- and multi-target detectors one could expect a dip which provides information about whether the new vector boson physics involves CP violating phases and—eventually—allows to extract information about its size. We have stressed that in a mono-target detector the exact position of the dip allows for the reconstruction of the coupling  $|H_V|$ , within an interval. The small spread of the dipoles for the different germanium isotopes allows the same reconstruction procedure in the multi-target case. An observation of a dip in the event rate spectrum will fix the value of  $|H_V|$  within an energy recoil isocontour up to the recoil energy resolution, in the NaI, Ge and LAr detectors.

We now turn to the discussion of the “no-dip zone” regions in the graphs in fig. 2. For that purpose we use the LAr detector (middle graph and detector parameters according to tab. I). As we have already mentioned, the observation of a dip places the possible parameters responsible for a signal within the upper triangles in the graphs in fig. 2. The question is then what

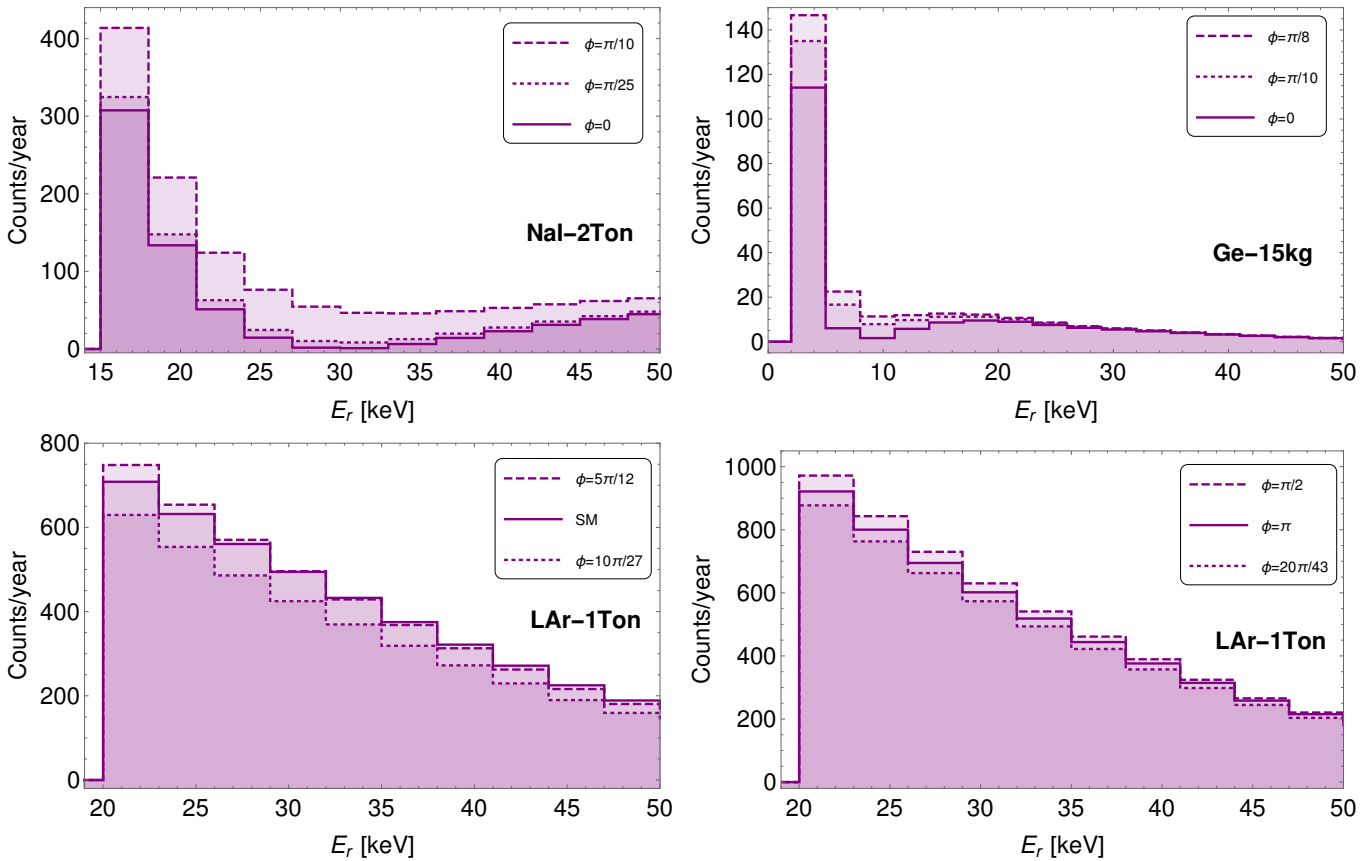


FIG. 3. **Upper left:** Event rate spectrum calculated in the NaI detector assuming one-year exposure and  $m_{\text{det}} = 2$  ton. The dip is obtained for  $\phi = 0$ , the presence of CP violation lifts the dip in such a way that the larger  $\phi$  the less pronounced the dip. Observation of these features can then be used to constrain the amount of CP violation involved by the new physics. **Upper right:** Same as in the NaI detector, but calculated for the germanium detector assuming full cancellation in  $^{74}\text{Ge}$  and  $m_{\text{det}} = 15$  kg. In this case the similarity of the five isotopes leads to dips for all of them that spread within a recoil energy interval of 2 keV. The set of dips within that narrow window leads to an overall dip as shown in the graph. **Lower left:** Degeneracy between the SM prediction and the SM+vector with  $\phi \neq 0$  in the LAr detector with  $m_{\text{det}} = 1$  ton. **Lower right:** Degeneracy between a spectrum generated with real parameters and spectra generated with  $\phi \neq 0$  in the LAr detector as well. These two cases, labeled SM degeneracy and real-vs-complex degeneracy, show that the interpretation of a CEvNS signal should be done including CP violating effects.

are the consequences of CP violating phases if the parameters  $\{m_V, |H_V|\}$  are located in the lower triangular region. With  $\phi = 0$  only the SM spectrum or a non-SM spectrum with real parameters can be generated. In the first case one would like to know whether a SM-like signal suffices to discard CP violation. In the second case, instead, what can be said about  $\phi$  from such a signal.

We generate the SM signal by fixing  $|H_V| = 0$  and then generate a set of signals using the parameter space point  $\{m_V, |H_V|\} = \{50\text{MeV}, 4.25 \times 10^{-7}\}$  for different values of  $\phi$ , as shown in the lower left graph in fig. 3. The value for  $|H_V|$  is obtained by fixing  $m_V = 50\text{MeV}$  in eq. (7) at  $E_r = 0\text{keV}$ . In general, for a point in either the boundary of the two regions or in the lower triangle the resulting spectra are rather different from the SM prediction. However, we find that for suitable values of  $\phi$  one can always find SM+vector spectra that degenerate to a large degree with that of the SM, as illustrated in the graph for  $\phi = 5\pi/12$  and  $\phi = 10\pi/27$ . Thus, we conclude that the observation of a SM-like signal cannot be

used to rule out CP violating interactions.

We then fix a spectrum generated with real parameters with the point  $\{m_V, |H_V|\} = \{16\text{MeV}, 4.45 \times 10^{-8}\}$  and  $\phi = \pi$ . As in the previous case we try to find spectra that degenerate with this one. For the point  $\{50\text{MeV}, 4.25 \times 10^{-7}\}$  (used in the case of SM degeneracy as well), we find that  $\phi = \pi/2$  and  $\phi = 20\pi/43$  generate spectra that follow rather closely the “real spectrum”. In summary, therefore, in the no-dip zone we find that the presence of CP violation leads to degeneracies that call for the inclusion of CP violating effects if CEvNS data is to be interpreted in terms of light vector mediators.

#### IV. DETERMINING THE SIZE OF CP VIOLATING EFFECTS

We have shown that the inclusion of CP violation has three main effects: (i) suppression of eventual dips in the event rate spectrum, (ii) degeneracy between the SM prediction and the

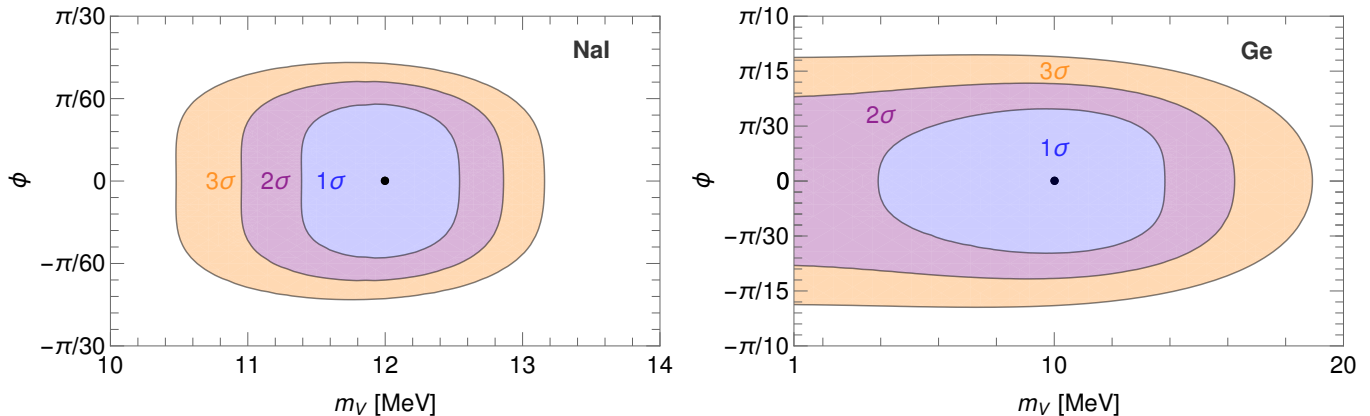


FIG. 4. **Left graph:** Results of the chi-square analysis for the NaI detector. The three regions correspond to the  $1\sigma$ ,  $2\sigma$  and  $3\sigma$  CL isocontours in the  $m_\nu - \phi$  plane. The contours show the degree at which a CEvNS signal involving a dip will allow to constrain the amount of CP violation. **Right graph:** Same as in the left graph but for the multi-target germanium detector. In this case the constraints on  $\phi$ , although still rather competitive, are less pronounced than in the NaI detector due to differences in the detector volume size. The black points indicate the best fit point value.

light vector mediator signal (SM degeneracy), (iii) degeneracy between spectra generated with real parameters and spectra including CP violating phases (real-vs-complex degeneracy). In what follows we study these three cases in more detail. We do so by taking four data sets that we treat as pseudo-experiments. With them we then perform a  $\chi^2$  analysis to show how much  $\phi$  can be constrained with experimental data. We assume a Poissonian distribution for the binned statistical uncertainty, and so we do not include any steady-state nor beam-on backgrounds.

#### A. The case of sodium and germanium detectors

To show the degree at which the presence of a dip can constrain the values of  $\phi$ , we do a counting experiment and perform a  $\chi^2$  analysis. For that we employ eq. (10) considering only the signal nuisance parameter and experimental signal uncertainty  $\sigma_\alpha$ , which we keep as in the COHERENT CsI phase. In both cases we use the neutrino fluxes from eq. (11) and we fix the remaining parameters according to tab. I. For the NaI detector we use  $H(E_r/\text{keV} - 15)$ , while for the germanium detector  $H(E_r/\text{keV} - 2)$ . The binning is done in such a way that the first data point is centered at  $E_r^{\text{th}}/\text{keV} + 1.5$ .

For the NaI analysis, the data points used for  $N_{\text{exp}}$  are obtained by fixing  $\phi = 0$  and the parameter space point shown in the left graph of fig. 2 (black point), with coordinates  $\{12\text{MeV}, 1.32 \times 10^7\}$ . As we mentioned in the previous section, that point generates a dip at  $E_r = 31\text{keV}$ . We then generated a set of spectra by varying  $m_\nu$  within  $[1, 100]\text{MeV}$  and  $\phi$  within  $[-\pi, \pi]$ , for the same  $|H_V|$ . The results of the  $\chi^2$  analysis are displayed in the left graph in fig. 4, which shows the  $1\sigma$ ,  $2\sigma$  and  $3\sigma$  CL isocontours in the  $m_\nu - \phi$ . From this graph it can be seen that an observation of a dip in the event spectrum in the NaI detector cannot rule out CP violating interactions, but can place tight bounds on  $\phi$ . For this particular analysis, all

values of  $\phi$  but those in the range  $[-\pi/60, \pi/60]$  are excluded at the  $1\sigma$  level, and increasing the CL does not substantially enlarge the allowed values. For the germanium detector we use as well the point used in the previous section (black point in the left graph in fig. 2 located at  $\{15\text{MeV}, 4.17 \times 10^{-7}\}$ ) to generate  $N_{\text{exp}}$ . The result of the  $\chi^2$  test is shown in the right graph in fig. 4. In this case, the constraints on  $\phi$  are as well competitive enough but are less tight than those found in the NaI case. They are about a factor  $\sim 2$  less stringent due to the difference in statistics. As the upper right and left histograms in fig. 3 show, the number of events in the NaI detector is way larger than in the germanium one. As a consequence the statistical uncertainties in NaI are less relevant than in Ge. Regardless of whether one includes or not the background, which increases the statistical uncertainty, this is a rather generic conclusion. The larger the detector the larger the range over which  $\phi$  can be excluded.

#### B. The case of the LAr detector

For the LAr detector we assume the parameters shown in tab. I and take for the acceptance function a Heaviside function  $H(E_r/20\text{keV} - 20)$ . We proceed basically in the same way that in the sodium and germanium detectors. For the SM degeneracy case  $N_{\text{exp}}$  is fixed with the SM prediction, while for the real-vs-complex degeneracy case the pseudo-experiment data set is generated fixing  $\phi$  to  $\pi$ ,  $|H_V|$  to  $4.45 \times 10^{-7}$  and  $m_\nu = 16\text{MeV}$ . For the  $\chi^2$  analysis we fix  $|H_V|$  to  $4.25 \times 10^{-7}$  and let both  $m_\nu$  and  $\phi$  vary.

The results for both analyses are shown in fig. 5. The left graph shows the  $1\sigma$ ,  $2\sigma$  and  $3\sigma$  CL regions for which degeneracy with the SM prediction is induced by complex parameters. The right graph shows the same exclusion regions for which complex parameters mimic an event rate spectrum involving only real parameters. As we have already stressed these re-



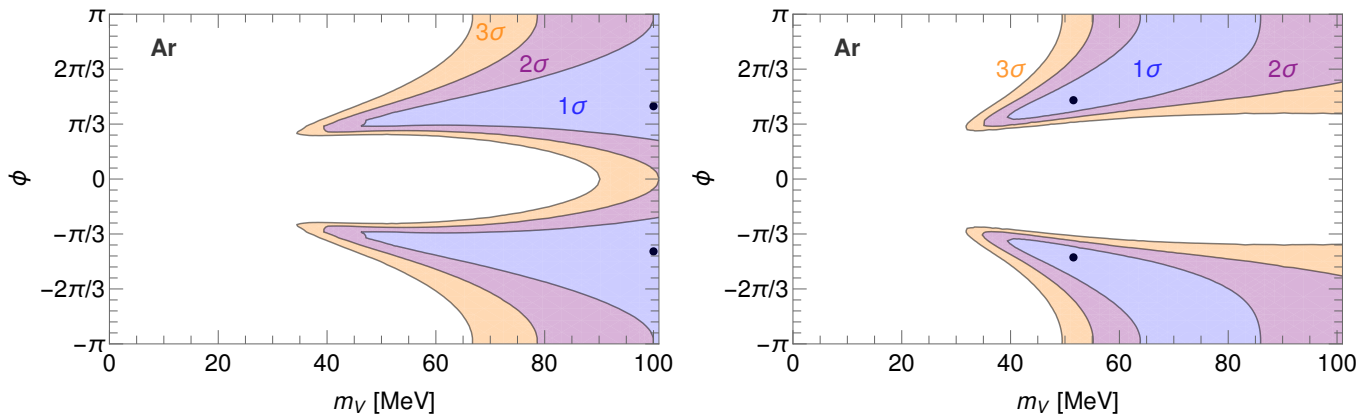


FIG. 5. Results of the chi-square analysis for the LAr detector. **Left graph:** Regions correspond to the  $1\sigma$ ,  $2\sigma$  and  $3\sigma$  CL isocontours in the  $m_V - \phi$  plane. The contours show the regions where CP violating parameters (encoded in the effective CP violating phase  $\phi$ ) mimic the SM event rate spectrum. **Right graph:** Same as in the left graph but for degeneracy between a spectrum generated with real parameters and spectra generated with CP violating parameters. The black points indicate the best fit point values in both cases.

sults should not be understood as what the actual experiments (or at least simulated data) will achieve, but they do demonstrate our point: Regions in parameter space exist in which CP violating phases can mimic signals that at first sight can be interpreted as either SM-like or entirely generated by real parameters. This analysis therefore allows to establish one of our main points, that is a fully meaningful interpretation of CEvNS data in terms of light vector mediators should come along with the inclusion of CP violating phases.

## V. CONCLUSIONS

We have considered the effects of CP violating parameters on CEvNS processes, and for that aim we have considered light vector mediator scenarios. First of all we have introduced a parametrization that reduces the—in principle—nine parameter problem to a three parameter problem. We have demonstrated that this parametrization proves to be extremely useful when dealing with CP violating effects. In contrast to light scalar mediator schemes, light vector mediators allow for interference between the SM and the new physics, something that we have shown enables the splitting of the parameter space into two non-overlapping sectors in which CP violating effects have different manifestations: (i) A region where full destructive interference between the SM and the new vector contribution leads to a dip in the event rate spectrum at a certain recoil energy, (ii) a region where CP violating parameters lead to degeneracies with either the SM prediction or with event rate spectra generated with real parameters.

We have shown that in case (i) information on the amount of CP violation can be obtained. A dip in the event rate spectrum will certainly not allow ruling out CP violation, but will allow to place—in general—stringent constraints on the CP violating effects, with the constraints being more pronounced

with larger detector volume. We have pointed out that the dip will as well provide information on the real effective coupling  $|H_V|$  responsible for the signal, it will enable its reconstruction with a 4% accuracy within an interval spanning about one order of magnitude. In case (ii) we have shown that fairly large regions in parameter space exist where CP violating parameters can mimic CP conserving signals (SM or signals originating from real parameters). We thus stress that meaningful and more sensitive interpretations of future CEvNS data in terms of light vector mediators should include CP violating parameters.

Finally, we point out that the results discussed here apply as well for CEvNS induced by reactor or solar/atmospheric neutrinos. Analyses of CEvNS data from these sources should include as well CP violating effects.

## ACKNOWLEDGMENTS

We would like to thank Danny Marfatia for reading the manuscript and for useful comments. To Grayson Rich for a very useful discussion on mono-target detectors as well as for providing information regarding different aspects of the COHERENT detectors. We also thank Pablo García and Dimitris Papoulias for useful discussions. DAS is supported by the grant “Unraveling new physics in the high-intensity and high-energy frontiers”, Fondecyt No 1171136. NR is funded by proyecto FONDECYT Postdoctorado Nacional (2017) num. 3170135. VDR acknowledges financial support by the “Juan de la Cierva Incorporación” program (IJCI-2016-27736) funded by the Spanish MINECO, as well as partial support by the Spanish grants FPA2017-90566-REDC (Red Consolider MultiDark), FPA2017-85216-P and SEV-2014-0398 (MINECO/AEI/FEDER, UE) and PROMETEO/2018/165 (Generalitat Valenciana).

- [1] D. Akimov et al. (COHERENT), *Science* (2017), 1708.01294.
- [2] *The CONUS Experiment*, [https://indico.cern.ch/event/606690/contributions/2591545/attachments/1499330/2336272/Taup2017\\_CONUS\\_talk\\_JHakenmueller.pdf](https://indico.cern.ch/event/606690/contributions/2591545/attachments/1499330/2336272/Taup2017_CONUS_talk_JHakenmueller.pdf).
- [3] A. Aguilar-Arevalo et al. (CONNIE), *J. Phys. Conf. Ser.* **761**, 012057 (2016), 1608.01565.
- [4] R. Strauss et al., *Eur. Phys. J.* **C77**, 506 (2017), 1704.04320.
- [5] E. Aprile et al. (XENON), *JCAP* **1604**, 027 (2016), 1512.07501.
- [6] D. S. Akerib et al. (LUX-ZEPLIN) (2018), 1802.06039.
- [7] J. Aalbers et al. (DARWIN), *JCAP* **1611**, 017 (2016), 1606.07001.
- [8] J. Billard, L. Strigari, and E. Figueroa-Feliciano, *Phys. Rev.* **D89**, 023524 (2014), 1307.5458.
- [9] B. Dutta and L. E. Strigari (2019), 1901.08876.
- [10] R. Harnik, J. Kopp, and P. A. N. Machado, *JCAP* **1207**, 026 (2012), 1202.6073.
- [11] D. G. Cerdeño, M. Fairbairn, T. Jubb, P. A. N. Machado, A. C. Vincent, and C. Boehm, *JHEP* **05**, 118 (2016), [Erratum: *JHEP*09,048(2016)], 1604.01025.
- [12] I. M. Shoemaker, *Phys. Rev.* **D95**, 115028 (2017), 1703.05774.
- [13] B. Dutta, S. Liao, L. E. Strigari, and J. W. Walker, *Phys. Lett.* **B773**, 242 (2017), 1705.00661.
- [14] D. Aristizabal Sierra, N. Rojas, and M. H. G. Tytgat, *JHEP* **03**, 197 (2018), 1712.09667.
- [15] M. C. Gonzalez-Garcia, M. Maltoni, Y. F. Perez-Gonzalez, and R. Zukanovich Funchal, *JHEP* **07**, 019 (2018), 1803.03650.
- [16] J. Billard, J. Johnston, and B. J. Kavanagh, *JCAP* **1811**, 016 (2018), 1805.01798.
- [17] D. Z. Freedman, *Phys. Rev.* **D9**, 1389 (1974).
- [18] D. Z. Freedman, D. N. Schramm, and D. L. Tubbs, *Ann. Rev. Nucl. Part. Sci.* **27**, 167 (1977).
- [19] V. A. Bednyakov and D. V. Naumov, *Phys. Rev.* **D98**, 053004 (2018), 1806.08768.
- [20] D. Aristizabal Sierra, J. Liao, and D. Marfatia (2019), 1902.07398.
- [21] D. Akimov et al. (COHERENT) (2018), 1804.09459.
- [22] P. Coloma, M. C. Gonzalez-Garcia, M. Maltoni, and T. Schwetz, *Phys. Rev.* **D96**, 115007 (2017), 1708.02899.
- [23] J. Liao and D. Marfatia, *Phys. Lett.* **B775**, 54 (2017), 1708.04255.
- [24] O. G. Miranda, G. Sanchez Garcia, and O. Sanders (2019), 1902.09036.
- [25] Y. Farzan, M. Lindner, W. Rodejohann, and X.-J. Xu, *JHEP* **05**, 066 (2018), 1802.05171.
- [26] D. K. Papoulias and T. S. Kosmas, *Phys. Rev.* **D97**, 033003 (2018), 1711.09773.
- [27] O. G. Miranda, D. K. Papoulias, M. Tórtola, and J. W. F. Valle (2019), 1905.03750.
- [28] D. Aristizabal Sierra, V. De Romeri, and N. Rojas, *Phys. Rev.* **D98**, 075018 (2018), 1806.07424.
- [29] J. B. Dent, B. Dutta, S. Liao, J. L. Newstead, L. E. Strigari, and J. W. Walker, *Phys. Rev.* **D96**, 095007 (2017), 1612.06350.
- [30] K. Scholberg, *COFI Seminar*, <https://pdfs.semanticscholar.org/b989/bb1f6ca0ec509e3415253cdefdd52f056f39.pdf> (2017), [Online; accessed 7-May-2019].
- [31] Y. Farzan, *Phys. Lett.* **B748**, 311 (2015), 1505.06906.
- [32] Y. Farzan and I. M. Shoemaker, *JHEP* **07**, 033 (2016), 1512.09147.
- [33] Y. Farzan and J. Heeck, *Phys. Rev.* **D94**, 053010 (2016), 1607.07616.
- [34] M. B. Wise and Y. Zhang, *Phys. Rev.* **D90**, 053005 (2014), 1404.4663.
- [35] C. Patrignani and P. D. Group, *Chinese Physics C* **40**, 100001 (2016), URL <http://stacks.iop.org/1674-1137/40/i=10/a=100001>.
- [36] I. Angeli and K. P. Marinova, *Atom. Data Nucl. Data Tabl.* **99**, 69 (2013).
- [37] M. Centelles, X. Roca-Maza, X. Vinas, and M. Warda, *Phys. Rev. Lett.* **102**, 122502 (2009), 0806.2886.
- [38] R. H. Helm, *Phys. Rev.* **104**, 1466 (1956).
- [39] M. Bauer, P. Foldenauer, and J. Jaeckel, *JHEP* **07**, 094 (2018), 1803.05466.
- [40] A. Anastasi et al. (KLOE-2), *Phys. Lett.* **B757**, 356 (2016), 1603.06086.
- [41] J. P. Lees et al. (BaBar), *Phys. Rev. Lett.* **113**, 201801 (2014), 1406.2980.
- [42] G. Inguglia, *PoS DIS2016*, 263 (2016), 1607.02089.
- [43] W. H. Bertl et al. (SINDRUM), *Nucl. Phys.* **B260**, 1 (1985).
- [44] M. S. Alam et al. (CLEO), *Phys. Rev. Lett.* **76**, 2637 (1996).
- [45] R. Aaij et al. (LHCb), *Phys. Rev. Lett.* **120**, 061801 (2018), 1710.02867.
- [46] D. Curtin, R. Essig, S. Gori, and J. Shelton, *JHEP* **02**, 157 (2015), 1412.0018.
- [47] W. Altmannshofer, S. Gori, M. Pospelov, and I. Yavin, *Phys. Rev. Lett.* **113**, 091801 (2014), 1406.2332.
- [48] S. Bilmis, I. Turan, T. M. Aliev, M. Deniz, L. Singh, and H. T. Wong, *Phys. Rev.* **D92**, 033009 (2015), 1502.07763.
- [49] J. A. Grifols and E. Masso, *Phys. Lett.* **B173**, 237 (1986).
- [50] J. A. Grifols, E. Masso, and S. Peris, *Mod. Phys. Lett.* **A4**, 311 (1989).
- [51] J. H. Chang, R. Essig, and S. D. McDermott, *JHEP* **09**, 051 (2018), 1803.00993.
- [52] J. H. Chang, R. Essig, and S. D. McDermott, *JHEP* **01**, 107 (2017), 1611.03864.
- [53] B. Müller, *Publ. Astron. Soc. Austral.* **33**, e048 (2016), 1608.03274.
- [54] E. Hardy and R. Lasenby, *JHEP* **02**, 033 (2017), 1611.05852.
- [55] A. E. Nelson and J. Walsh, *Phys. Rev.* **D77**, 033001 (2008), 0711.1363.
- [56] A. E. Nelson and J. Walsh, *Phys. Rev.* **D77**, 095006 (2008), 0802.0762.